Pergamon

Acta Materialia 50 (2002) 1197–1209

Acta MATERIALIA

www.actamat-journals.com

On the interface debond at the edge of a thin film on a thick substrate

B. Erdem Alaca, M.T.A. Saif, Huseyin Sehitoglu *

Mechanical and Industrial Engineering, University of Illinois, 1206 West Green Street, Urbana, IL 61801, USA

Received 16 August 2001; received in revised form 6 November 2001; accepted 6 November 2001

Abstract

The failure by debonding of 400 nm Al thin films on 152 μm-thick polyimide substrates has been studied in uniaxial tension experiments. To explain the edge debond of the Al film, the shear stress field along the film–substrate interface is determined. An analytical solution for the stress field exhibits a square root singularity near the free edges. The associated stress intensity factor is calculated in closed form by an asymptotic analysis. For a given loading, the stress intensity factor decreases with increasing length-to-thickness ratio of the film, and with decreasing film-to-substrate stiffness ratio. Governed by a single, dimensionless parameter, these trends are reported quantitatively in the form of a plot. Close correspondence is found for the interfacial shear stresses predicted by the presented method and by a finite element analysis. © 2002 Acta Materialia Inc. Published by Elsevier Science Ltd. All rights reserved.

Keywords: Thin films; Multilayers; Surfaces & interfaces; Nanofilms; Interface failure; Theory & modeling; Structural behavior

1. Introduction

One of the common modes of failure of thin film–substrate structures is the ‘edge debond’, the delamination of thin film at a free edge. Many experimental observations of this phenomenon have been reported. For example, Bagchi et al. [1] studied residual stress-driven delamination between copper films and silica substrates originating at the free edge of the film. At the free edge, an additional layer of carbon between copper and silica facilitated the onset of delamination due to its poor adherence characteristics. Chiu et al. [2] tested gold strips on polyimide substrates with a thin chromium inter-layer to enhance adhesion. When the polyimide substrate was subjected to uniaxial tension, delamination was observed to start from free edges of gold strips. Furthermore, Ogawa et al. [3] observed Mode II interfacial cracks at the edge of TiN films deposited on steel substrates, where the substrate was under compressive loading.

Theoretical treatments of the problem can be divided into two groups. It is either assumed that a pre-existing edge defect in the form of a sharp crack is a precursor to an edge debond [4,5], or it is assumed that interface at the edge is perfect and the edge debond occurs due to stress singularity at the free edge [6]. The latter concerns the initiation of an interfacial crack, whereas the former

* Tel.: +1-217-333-3859; fax: +1-217-244-6534.
E-mail address: huseyin@uiuc.edu (H. Sehitoglu).

PII: S1359-6454(01)00421-9

approach considers the edge debond as the propagation of an existing crack, although, in reality, it is very difficult to determine the size of this initial flaw. Depending on the characteristics of the particular application of interest, one method should be preferred over the other. A comparison of the implications of both methods when applied to a bimaterial strip is given by Klingbeil and Beuth [7].

Considerable progress has been made with the edge flaw method, especially with the recent analysis by Yu, He and Hutchinson [5], which addresses fundamental aspects, such as energy release rate and mode mixity, associated with an interfacial crack at the edge. However, the lack of a pre-existing crack can be of crucial importance in certain cases. Therefore the present study treats the problem of a thin film of finite width bonded to a substrate without assuming any interfacial pre-crack. This is achieved by investigating singular stress fields at the free edge of the thin film.

Among the many studies on singularities for edge debond problems [8–13], the work by Erdogan and Gupta [8] is one of the earliest and most relevant to thin films, where singular shear stresses between an elastic stiffener and a half plane are determined by solving a compatibility equation in the form of a singular integral equation. Later, Shield and Kim [14] extended this analysis by imparting bending stiffness to the film to incorporate normal tractions in addition to interfacial shear. However, both analyses employ a series approximation method making the solution procedure difficult to apply to a specific case of interest. Although the present work deals with similar integral equations, these are solved in closed form in contrast to earlier works. This is achieved by noting the similarity between the governing integro-differential equation for the interfacial shear and Prandtl's integro-differential equation, that governs the circulation of air flow around a wing of finite span in aerodynamics [15]. Vekua's solution procedure of Prandtl's equation, given in [16], is adopted and shear stress distribution between a thin film of finite dimensions and its substrate is found in closed form, thereby eliminating numerical issues related to earlier works, including convergence.

In addition to supplying a closed-form solution, the present work also provides a clear discussion on the range of applicability of this method. Since neglecting bending stiffness of the thin film results in inaccurate shear stress predictions for certain material combinations, the determination of a well-defined limit, beyond which the deviation of the predictions from real values is not acceptable, becomes a necessity. Such a distinction, missing in the previous literature, is also established here.

The motivation of the present work is an electrostatically actuated micro pump [17]. The actuator consists of a silicon cavity and a composite diaphragm, which is essentially a polymeric substrate with dielectric and conducting coatings. Upon actuation, fluid in the cavity is pressurized by the diaphragm and when a critical pressure is reached, fluid is pumped out. During this process the diaphragm is strained. A possible mechanism of failure of the diaphragm is cracking in the metallic coating and subsequent delamination of film edge from polymeric substrate.

To study such failure mechanisms, uniaxial tensile tests are carried out with specimens consisting of stiff films on compliant substrates, where in-situ optical microscopy revealed crack formation in the film accompanied by delamination emanating from free edges. Using experimental measurements and in-situ observations as input data for the theory developed here, one can determine critical stress intensity factors for delamination.

2. Experimental results and observations

To study the failure of stiff coatings on compliant substrates, uniaxial tensile tests are carried out on Al-coated Kapton™ Type-HN (trademark of DuPont Company) aromatic polyimide PMDA-ODA substrates. Kapton™ films with a thickness of 152 μm are cleaned first with acetone and then with isopropyl alcohol and blown-dry with nitrogen. Cleaned films are cut into 10 mm-by-100 mm rectangular strips, and a 400 nm-thick Al layer is deposited on strip surfaces in an RF sputtering system.

The monotonic tensile test is conducted on a screw-driven Instron Mini44 with a 500 N load cell. 20 mm from each end of the specimen is left for gripping. Pneumatic grips with flat rubber faces, which can accommodate the thickness change of the specimen during the test and hence prevent the specimen from slipping, are used. Strains are calculated based on cross-head displacement. Two leads attached to each end of the specimen are employed to measure the resistance change of Al coating during the test, while an optical microscope is used for in-situ observations.

The resulting engineering stress–strain curve is given in Fig. 1, where the average strain rate is $3 \times 10{-}4\ s^{-1}$. There is no definite yield point and the material deforms uniformly without necking, a characteristic of Kapton™. Crack formation is observed in the Al film perpendicular to the direction of loading dividing the Al film into many strips as depicted in Fig. 2. Crack formation is also monitored by resistance measurements shown in Fig. 3. A steep increase in resistance is observed, which indicates that a heavy crack formation takes place at early stages of the test, even though cracks are too small to be observed via microscope. Upon further stretching, separation between newly formed Al strips increases accompanied by the formation of new cracks. This kind of crack formation

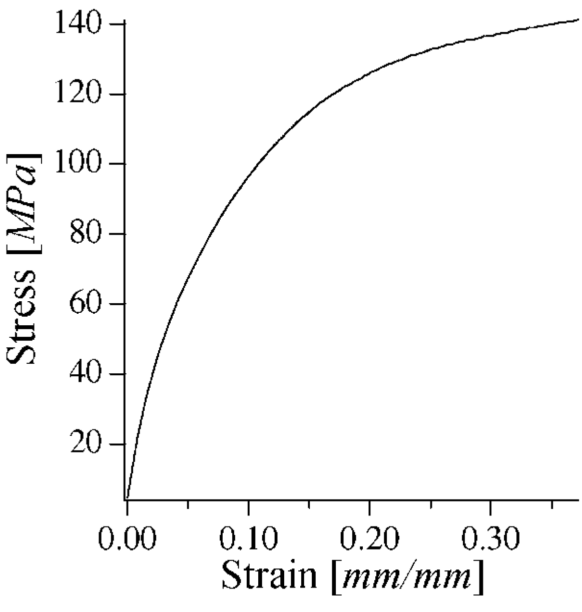

Fig. 1. Uniaxial stress–strain response of a 152 μm-thick polyimide substrate coated with 400 nm-thick Al film.

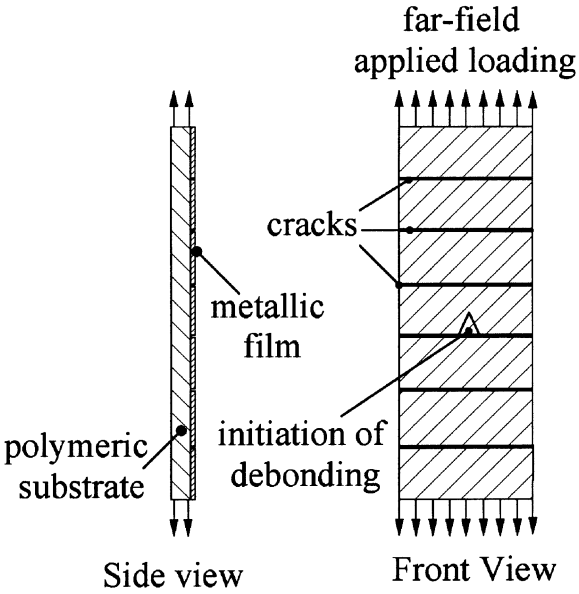

Fig. 2. Schematic of a uniaxial tension test sample consisting of a thick polymeric substrate and a thin metallic film. When the substrate is stretched, cracks form in the film perpendicular to stretch direction followed by the initiation of debonding of the metallic film at the free edge of each strip formed by two of such cracks.

was previously observed by Agrawal and Raj [18] and used to determine shear strength of a ceramic–metal interface.

The second stage of deformation involves an additional phenomenon: delamination. At 6% strain, the Al coating starts spalling off. Micrographs in Figs. 4 and 5 show a specimen at this stage. Using in-situ microscopy, delamination of the Al film is observed to start at the cracked edge of each strip, where, being a free edge, the Poisson's contraction which the substrate is undergoing cannot be accommodated by the metallic strip, and hence, lateral compressive stresses arise leading to the buckling of the Al coating. Driven by buckling, delamination propagates through the width of the strip and gets arrested at the other edge. This is a very fast process that cannot be captured with 1/60 s frames, and during this propagation, the width of the delaminated region decreases resulting in the trapezoidal shapes of Figs. 4 and 5. Buckled portions of the Al film break at the top and occasionally the whole film spalls off exposing the underlying polyimide substrate.

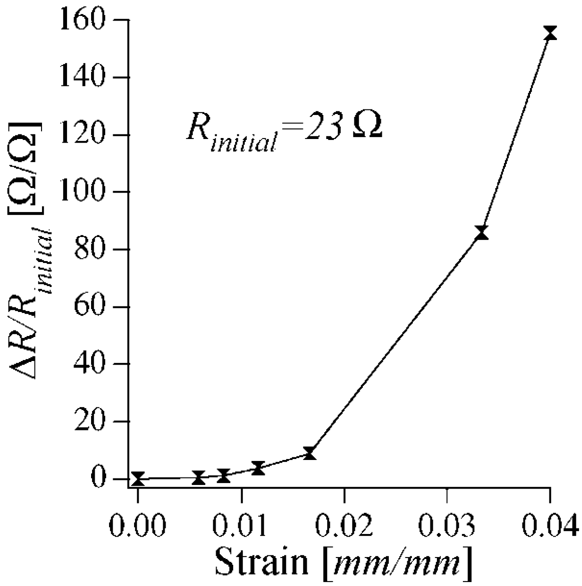

Fig. 3. The change of resistance across the Al film is monitored during the uniaxial experiment. Here the change of resistance, ΔR, normalized by the initial resistance is plotted against strain. The steep change suggests that a heavy formation of cracks in the Al film takes place at early stages of the test.

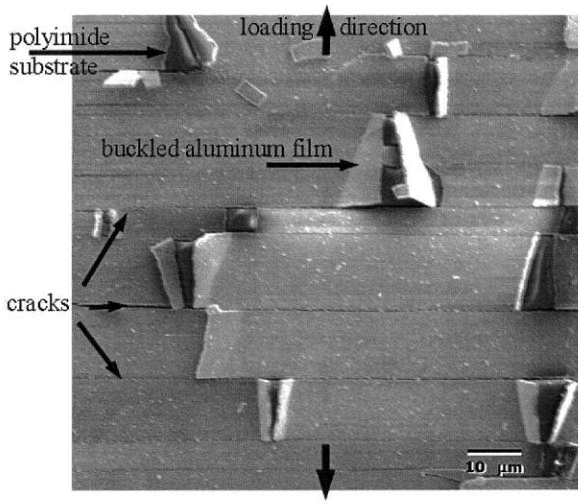

Fig. 4. Micrograph of a tension test sample consisting of a 152 µm-thick Kapton™ substrate coated with a 400 nm Al thin film. Cracks develop in the Al film perpendicular to loading direction. Upon further stretching, delamination starts at the free edge of a strip between two such cracks and propagates towards the other edge. Since the delamination is buckle-driven, it indicates that an initially debonded region has to exist at the interface. In this work, this initial debonding is treated as an interface failure due to singular stress fields near the free edge.

To demonstrate the effect of interface properties on delamination, a second set of specimens is fabricated with an additional, 10 nm-thick Cr layer as an adhesion promoter between polyimide and Al. In this case, delamination and buckling are still evident, however, the size of delaminated regions is much smaller in scale as shown in Fig. 6. Since buckling is observed in each case and since an initially debonded area is required for buckling, the mechanism by which debonding occurs is sought in this paper by investigating the stress field along the interface. Experimental results will be used along with the theory developed in the next section to find critical stress intensity factors for delamination.

3. Theory

3.1. Statement of the problem

The plane elasticity problem considered in this work is depicted in Fig. 7. Homogeneous, isotropic, linear elastic, thin film has a symmetric profile around the y-axis. It has a length of $2a$ and a variable thickness of $b(x)$. Elastic modulus and Poisson's ratio of the film are designated as E_f and ν_f, respectively. Homogeneous, isotropic, linear elastic substrate is semi-infinite and under a uniform, uniaxial far-field stress, σ^0. Substrate's elastic modulus and Poisson's ratio are given as E_s and ν_s, respectively.

An infinitesimal slice of thin film is shown in Fig. 8 with all the forces acting on it. At this point, it is assumed that Z_x, normal force per unit width of the film in the x-direction, is uniform across the thickness. The change in Z_x is balanced by the interfacial shear, $\tau(x)$. This shear lag assumption then leads to the following equilibrium equation for the thin film:

$$\frac{\mathrm{d}Z_x}{\mathrm{d}x} = \tau(x) \tag{1}$$

Hence, the normal stress in the film, σ_x^f, can now be expressed as follows:

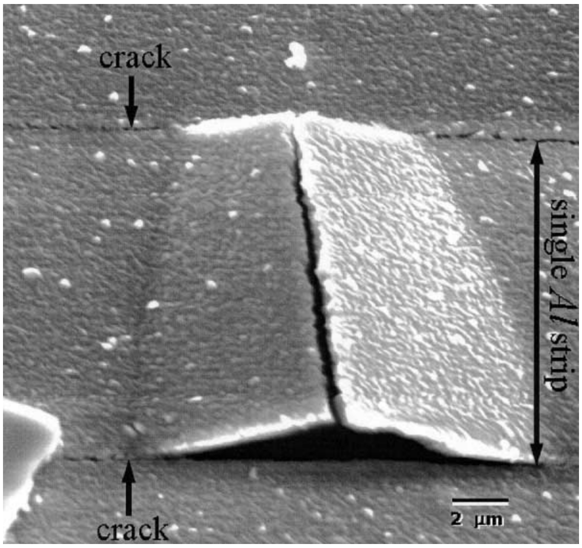

Fig. 5. Micrograph showing details of delamination in a single Al strip between two cracks. Accompanied by buckling, the delamination emanates from the lower edge of the strip, where it is wider, and propagates towards the upper edge. Buckled metallic film does not spall off in this case, but it breaks at the top due to excessive deformation.

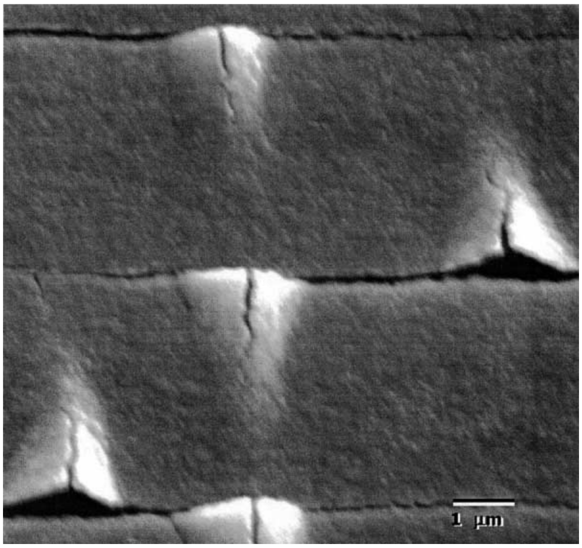

Fig. 6. The extent of delamination is determined by interface properties. Here the effect of the addition of a 10 nm Cr layer as an adhesion promoter between polyimide and Al is demonstrated. The size of delaminated regions is much smaller than those shown in Figs. 4 and 5.

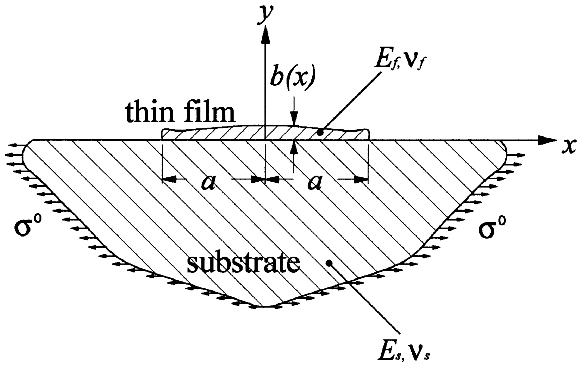

Fig. 7. Thin film–substrate configuration of the plane elasticity problem. Thin film has a symmetric profile around the y axis. Its length is $2a$ and it has a variable thickness of $b(x)$. The substrate is semi-infinite and under uniform, uniaxial far-field stress, σ_0. Both media are homogeneous, isotropic and linear elastic with elastic moduli designated as E_s, E_f, and Poisson's ratios designated as ν_s, ν_f for the substrate and the film, respectively.

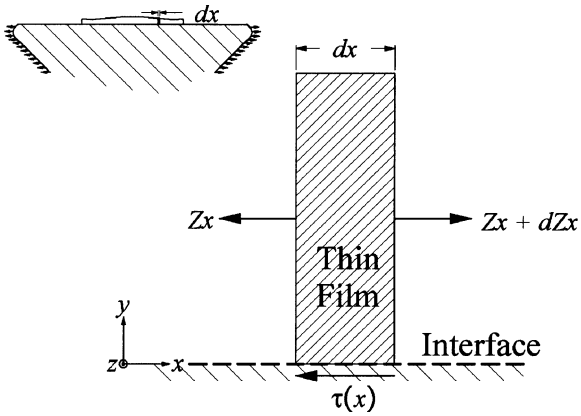

Fig. 8. Shear lag model shown on a slice of thin film of length dx. The infinitesimal change in the normal force per unit width of the thin film in the x-direction, Z_x, is balanced by the interfacial shear, $\tau(x)$.

$$\sigma_x^{\mathrm{f}} = \frac{Z_x}{b(x)} = \frac{1}{b(x)}\int_{-a}^{x} \tau(s)\mathrm{d}s \tag{2}$$

On the other hand, σ_x^{s}, normal stress in the substrate immediately below the interface, can be written as [19]

$$\sigma_x^{\mathrm{s}}\big|_{y=0} = \frac{2}{\pi}\int_{-a}^{a} \frac{\tau(s)}{s-x}\mathrm{d}s + \sigma^0 \tag{3}$$

Since film thickness is small and its top surface is traction-free ($\sigma_y = 0$), it is assumed that σ_y is negligible across the thickness of the film. Furthermore, assuming plane strain in the z direction, we can write corresponding linear elastic strains, ϵ_x^f and ϵ_x^s, in the film and in the substrate, respectively, as follows:

$$\epsilon_x^f = \frac{1-\nu_f^2}{E_f}\frac{1}{b(x)}\int_{-a}^{x}\tau(s)\mathrm{d}s \tag{4}$$

$$\epsilon_x^s = \frac{1-\nu_s^2}{E_s}\left(\frac{2}{\pi}\int_{-a}^{a}\frac{\tau(s)}{s-x}\mathrm{d}s + \sigma^0\right) \tag{5}$$

If we consider a perfect bonding of the two materials, displacements in x and y directions should be continuous across the interface. The continuity of the displacement in the x direction can also be described in terms of strains, and hence a compatibility equation can be written:

$$\epsilon_x^f = \epsilon_x^s|_{y=0} \tag{6}$$

Using Eqs. (4) and (5), Eq. (6) can be rewritten as:

$$\frac{1}{b(x)}\int_{-a}^{x}\tau(s)\mathrm{d}s + A\int_{-a}^{a}\frac{\tau(s)}{x-s}\mathrm{d}s = F \tag{7}$$

where

$$A = \frac{2}{\pi}\frac{1-\nu_s^2}{1-\nu_f^2}\frac{E_f}{E_s} \tag{8}$$

and

$$F = \frac{1-\nu_s^2}{1-\nu_f^2}\frac{E_f}{E_s}\sigma^0 \tag{9}$$

The forcing function, F, of Eq. (7) can be derived for different cases making the solution method of this work applicable not only to the specific case discussed here, namely the case of substrate under uniform tension, but to many others. For example, thermal mismatch is an unavoidable outcome of thin film deposition which requires elevated temperatures. When the layered material is cooled down to room temperature after the deposition, the difference between the coefficients of thermal expansion of substrate and film, α_s and α_f, respectively, leads to the development of thermal residual stresses. In this case, Eq. (7) still represents the compatibility, but this time with the new forcing function, F, which, under plane strain condition, can be written as

$$F = (\alpha_s(1+\nu_s)-\alpha_f(1+\nu_f))\frac{E_f}{1-\nu_f^2}\Delta T \tag{10}$$

where ΔT designates the change in temperature associated with cooling.

Compatibility equation, Eq. (7), is an integro-differential equation with the interfacial shear, $\tau(x)$, being the unknown. This equation will be solved analytically in the next section.

3.2. Determination of interfacial shear

Eq. (7) can be rewritten in the following form:

$$\frac{1}{Ab(x)}\Gamma(x) - \int_{-a}^{a}\frac{\Gamma'(s)}{s-x}\mathrm{d}s = f \tag{11}$$

where $\Gamma(x) = \int_{-a}^{x}\tau(s)\mathrm{d}s$ and $\Gamma'(x)$ is its derivative with respect to x, which is identical to the shear stress distribution, $\tau(x)$, and

$$f = \frac{F}{A} \tag{12}$$

A similar form of Eq. (11) was solved by Vekua [16] in the context of the theory of aircraft wings with finite dimensions. In Appendix A, main steps of Vekua's method are summarized, which involve the reduction of Eq. (11) to the following Fredholm equation of the second kind:

$$\Gamma(x) - \int_{-a}^{a}K(x,\sigma)\Gamma(\sigma)\mathrm{d}\sigma = g(x) \tag{13}$$

where $g(x)$ is defined in Appendix A. In order to solve $\Gamma(x)$ analytically, a specific choice of the kernel, $K(x,t)$, is required. This, in turn, is achieved by using the following functional form for the thickness profile, $b(x)$:

$$b(x) = b_0\sqrt{1-\frac{x^2}{a^2}}\left(1 + \nu\frac{x^2}{a^2}\right) \tag{14}$$

This gives a nearly rectangular thickness profile as shown in Fig. 9, where the shape parameter $\nu = 0.9$ and b_0 is the thickness in the middle of the film such that $b(x)\approx b_0$. With $b(x)$ defined by Eq. (14), $K(x,t)$ takes the following form:

$$K(x,t) = \frac{(\chi/\pi)\nu t}{a^2 + \nu t^2}\varphi_1(x) + \frac{(\chi/\pi)\nu}{a^2 + \nu t^2}\varphi_2(x) \tag{15}$$

where φ_i are defined in Appendix A and

$$\chi = \frac{1}{2m}\frac{a}{b_0},\ m = \frac{E_f}{E_s}\frac{1-\nu_s^2}{1-\nu_f^2} \tag{16}$$

Using $K(x,t)$ of Eq. (15) in Eq. (13) gives the following solution for $\Gamma(x)$:

$$\Gamma(x) = g(x) + \frac{\frac{\chi}{\pi}\nu\int_{-a}^{a}\frac{g(\sigma)}{a^2 + \nu\sigma^2}\mathrm{d}\sigma}{1-\frac{\chi}{\pi}\nu\int_{-a}^{a}\frac{\varphi_2(\sigma)}{a^2 + \nu\sigma^2}\mathrm{d}\sigma}\varphi_2(x) \tag{17}$$

if the following relations hold:

$$\Gamma(x) = \Gamma(-x),\ b(x) = b(-x) \tag{18}$$

In addition to the conditions given in Eq. (18), f should also be constant. If f is not constant, as it is the case for localized heating [19] for example, the same method can still be used as long as f is an even function of x [16].

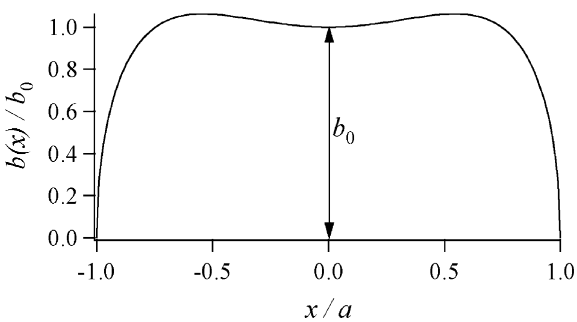

Fig. 9. A nearly rectangular film profile corresponding to shape parameter $\nu = 0.9$. Choosing a certain functional form for the film profile enables one to obtain a closed-form solution for interfacial shear stress.

Misprints in Eqs. (15) and (17) in the original work of Vekua [16] are corrected here. After $\Gamma(x)$ is found, its derivative is taken to find the shear stress distribution:

$$\tau(x) = \frac{\mathrm{d}\Gamma(x)}{\mathrm{d}x} \tag{19}$$

Rewriting $x = \xi a$, where ξ is non-dimensional, $\tau(\xi)$ can be expressed as:

$$\tau(\xi) = -\frac{f}{\pi}\frac{1}{\sqrt{1-\xi^2}} \left\{\frac{\chi}{1 + \nu\xi^2}\left[I_1(\xi) + \frac{I_2}{\cos\left[\frac{\chi}{\sqrt{1 + \nu}}\frac{\pi}{2}\right]}\sin[\theta(\xi)]\right] + \xi + \frac{C_1}{C_2}\frac{1}{1 + \nu\xi^2} \left[\chi\left(I_3(\xi) + \frac{I_4}{\cos\left[\frac{\chi}{\sqrt{1 + \nu}}\frac{\pi}{2}\right]}\sin[\theta(\xi)]\right) + \xi\right]\right\} \tag{20}$$

where $\theta(\xi)$, I_i, $i = 1, 4$ and C_i, $i = 1, 2$ are defined in Appendix B.

For a given forcing function, f, and film shape, ν, χ of Eq. (16) is the only parameter governing the interfacial shear stress, $\tau(\xi)$, in Eq. (20). Since χ is a dimensionless parameter incorporating material mismatch and film geometry, various film–substrate systems under the same loading and with different material combinations and film dimensions are expected to exhibit the same interfacial shear stress distribution, as long as χ is kept constant. More discussion on the universal characteristic of χ will be supplied in the next section.

Now let us consider the case of aluminum film on polyimide substrate, the system shown in Fig. 4. Then $E_f/E_s = 28$ and $\nu_f\approx\nu_s$. Al coating has a nearly rectangular profile, i.e. $\nu = 0.9$ (Fig. 9) with an aspect ratio of $a/b_0 = 16$, leading to $\chi = 0.286$. The substrate is under uniform tensile stress, σ^0, so that from Eqs. (8), (9) and (12), $f = \pi\sigma^0/2$. Integrations in Eq. (20) were carried out numerically using Mathematica (trademark of Wolfram Inc.) and the resulting shear stress distribution given by Eq. (20) is plotted in Fig. 10. In this plot shear stress is non-dimensionalized by the applied stress, σ^0, and the position, x, is non-dimensionalized by the half-span, a. It is clear from this plot that shear stress is nearly zero everywhere except for the close proximity of the edges, where it quickly builds up.

Eq. (20) reveals a square root singularity for the interfacial shear near the edges $x = \pm a$. Therefore fracture mechanics concepts, such as the Mode II stress intensity factor, K_{II}, can directly be utilized in this problem. In the remainder of the paper, K_{II} will directly be inferred from Eq. (20). But first it is necessary to justify the assumptions made to obtain interfacial shear stress distribution, namely shear lag assumption of Eq. (1) and approximating a rectangular profile by Eq. (14). This will be pursued in the following section using the finite element method.

4. Comparison with finite element results

Finite element calculations are carried out using ABAQUS (Trademark of Hibbitt, Karlsson & Sorensen, Inc.). 4204 quadrilateral elements with eight nodes are used under plane strain. Due to the symmetry of the problem, only half of the problem geometry is modeled as shown in Fig. 11. Here the substrate is 94 times thicker and 9 times longer than the coating. To verify theoretical results, aluminum and polyimide material properties are used such that $E_f/E_s = 28$ and $\nu_s \approx \nu_f$. Furthermore, thin film has a perfectly rectangular profile as shown in Fig. 11 with an aspect ratio $a/b_0 = 16$. Under these conditions, $\chi = 0.286$ according to Eq. (16). A uniaxial far-field stress is applied to the

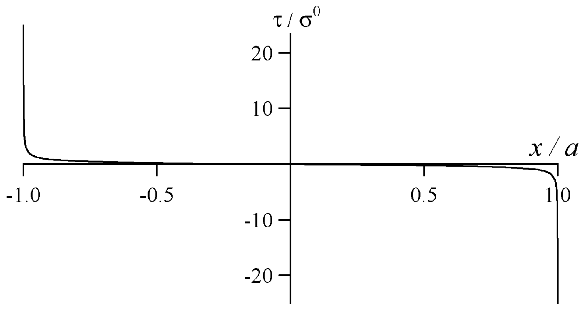

Fig. 10. Interfacial shear stress distribution for a thin film–substrate system with $E_f/E_s = 28$ and $\nu_f = \nu_s$. Thin film has a nearly rectangular profile (Fig. 9) with an aspect ratio of $a/b_0 = 16$. Interfacial shear, τ, is non-dimensionalized by the applied far-field stress, σ^0, in the substrate, and it is plotted against position x, non-dimensionalized by the half-span, a. Interfacial shear is almost non-existent except for the close proximity of free edges, where $x = \pm a$.

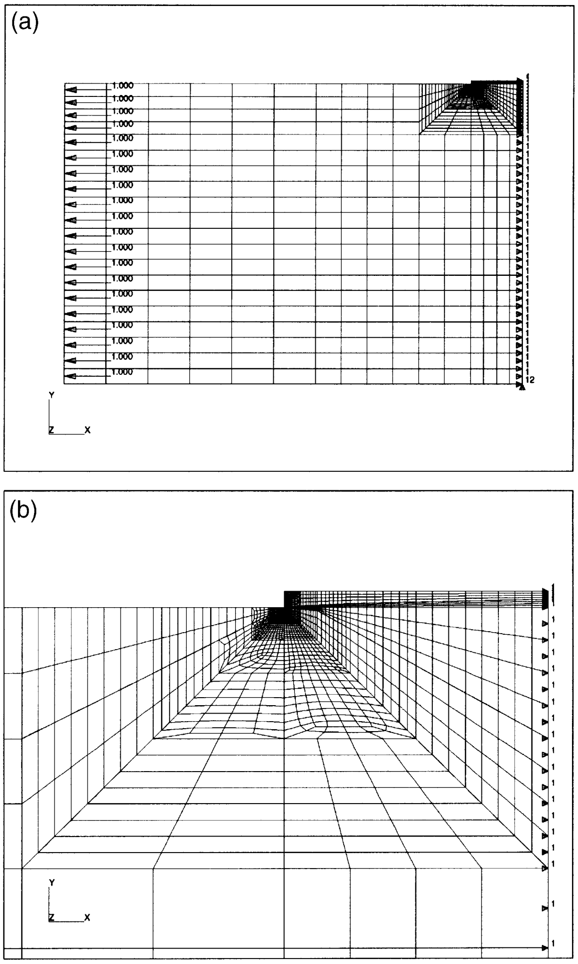

Fig. 11. Top: Finite element mesh used to model half of the problem geometry. Uniform far-field loading is shown on the left-hand side with arrows. Right-hand side has displacement boundary conditions due to symmetry. Bottom: A closer look at the finite element mesh near the free edge showing rectangular thin film and part of substrate lying directly beneath it.

substrate. Calculated shear stress is extrapolated to the nodes on the interface.

Fig. 12 shows interfacial shear stress obtained both from finite element analysis and from Eq. (20) plotted on a log scale. The slope of the linear regime of the finite element result, designated as the 'K-field', almost coincides with that from the theory verifying the square root singularity. Towards the free edge, however, a deviation is observed in the last few elements, which is an unavoidable result of using a sharp corner. It is well known that even a refined mesh will not yield accurate results close to this singular point [20].

Furthermore, two different meshes with different material properties are created, where χ is kept constant. The universality of χ is then investigated by comparing interfacial shear stress distributions of both meshes. The first mesh is the same as that given in Fig. 11 with $a/b_0 = 16$. The material mismatch is such that $E_f/E_s = 10$ and $\nu_s = \nu_f$. This gives $\chi = 0.8$. By increasing the length of the thin film of the first mesh ten times and keeping its thickness constant, a second mesh is obtained, where $a/b_0 = 160$. The substrate is made longer and thicker, accordingly. The near-field configuration is still given by Fig. 11. The stiffness ratio is also increased ten times to keep χ constant at 0.8 according to Eq. (16). Interfacial shear stresses for both meshes along with the theoretical prediction for $\chi = 0.8$ are plotted in Fig. 13. The close agreement exhibited by these plots is a verification of the universal characteristic of χ.

Since the primary motivation of this work is a micro pump, where a polymeric substrate is coated with a thin metal film, the material mismatch is always such that $E_f/E_s \gg 1$. Up to now, using such ratios, a good correspondence is observed between theory and finite element analysis in Figs. 12 and 13. However, to prove the validity of the square root singularity in general, this is not enough. Therefore, two extreme cases with $E_f/E_s = 1$ and 1000 are considered. For these calculations, the mesh with $a/b_0 = 16$ is used and the results are shown in Fig. 14. It is clear from this figure that with a ratio of 1, there is a poor agreement with theory, which becomes perfect for $E_f/E_s = 1000$. The explanation of this behavior is straightforward: in reality, normal tractions along the interface also have a singularity at the free edge, which is neglected in the present analysis. Since the film possesses a bending stiffness, these tractions will create moments and the behavior of the film will change especially near free edges. Furthermore, as also noted by Shield and Kim [14], these bending effects will diminish with increasing E_f, and hence the deviation between theory and finite element analysis will become negligible for stiffer films. Results of this section have shown that this is the case as long as the film is at least ten times stiffer

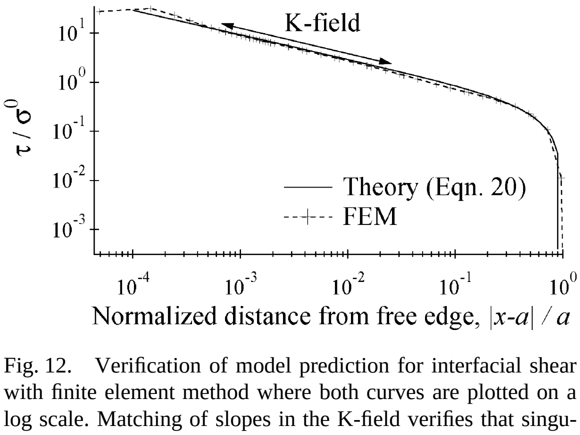

Fig. 12. Verification of model prediction for interfacial shear with finite element method where both curves are plotted on a log scale. Matching of slopes in the K-field verifies that singularity is very close to 0.5 as suggested by Eq. (20). The last few elements near the free edge exhibit an irregular behavior due to the fact that in the vicinity of the singular point, i.e. the sharp corner, finite element method will not give accurate results.

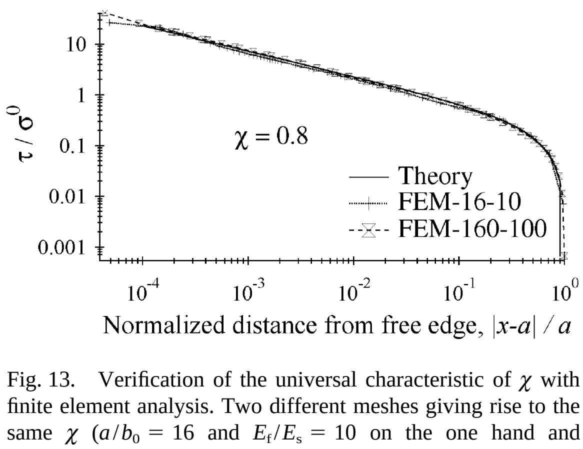

Fig. 13. Verification of the universal characteristic of χ with finite element analysis. Two different meshes giving rise to the same χ ($a/b_0 = 16$ and $E_f/E_s = 10$ on the one hand and $a/b_0 = 160$ and $E_f/E_s = 100$ on the other hand) exhibit the same shear stress distribution predicted by Eq. (20) of the theory.

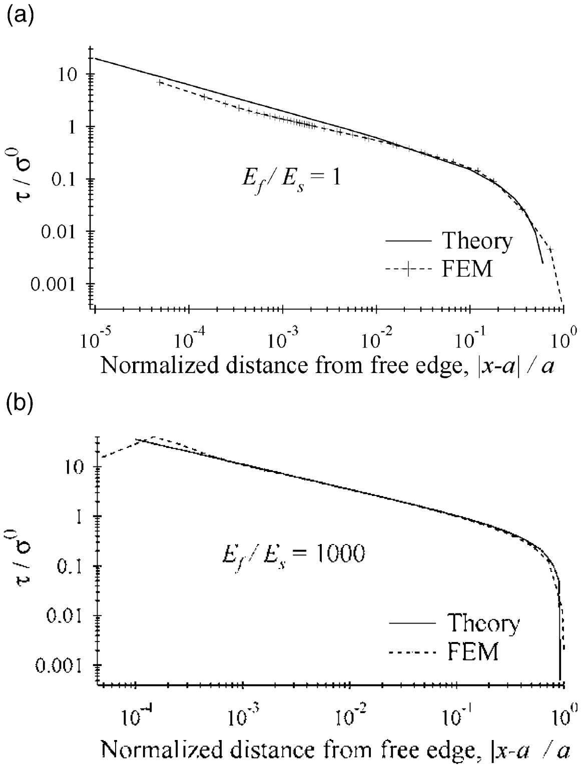

Fig. 14. Top: Comparison of theory and finite element result for $E_f/E_s = 1$ and $a/b_0 = 16$. Bottom: Same comparison for the extreme case of $E_f/E_s = 1000$.

than its substrate. Thus, having determined the domain of validity of the model, the K-field will be studied in detail in the following section.

5. Mode II stress intensity factor

Mode II stress intensity factor, K_{II}, is defined below:

$$K_{II} = \lim_{x\to -a}\left(\sqrt{2\pi(x+a)}\tau(x)\right) \tag{21}$$

Using Eq. (20) in this definition yields the following expression for K_{II}:

$$K_{II} = -\frac{f\sqrt{a}}{\sqrt{\pi}}\left\{\frac{\chi}{1+\nu}\left[I_1(-1) + \frac{I_2}{\cos\left[\frac{\chi}{\sqrt{1+\nu}}\frac{\pi}{2}\right]}\sin\left[-\frac{\chi}{\sqrt{1+\nu}}\frac{\pi}{2}\right]\right] -1 + \frac{C_1}{C_2}\frac{1}{1+\nu}\left[\chi\left(I_3(-1) + \frac{I_4}{\cos\left[\frac{\chi}{\sqrt{1+\nu}}\frac{\pi}{2}\right]}\sin\left[-\frac{\chi}{\sqrt{1+\nu}}\frac{\pi}{2}\right]\right)-1\right]\right\} \tag{22}$$

where individual functions, $I_1(-1)$, I_2, C_1, C_2, $I_3(-1)$ and I_4 are defined in Appendix B.

At this point, the universality of χ can be utilized in the following way: once the shape parameter, ν, is fixed in Eq. (22), K_{II} depends only on the forcing function, f, and on χ, which, according to Eq. (16), contains all the relevant geometric and material parameters. Therefore a single plot of the normalized $K_{II}/f\sqrt{a}$ as a function of χ can be used for a large class of loading conditions and material combinations. This plot is given in Fig. 15, from where some trends in the stress intensity factor can easily be deducted: $K_{II}/f\sqrt{a}$ decreases monotonically with increasing χ, i.e. it decreases with increasing length-to-thickness ratio of the film or with decreasing film-to-substrate stiffness ratio. When $\chi = 0$, it attains its maximum value of $1/\sqrt{\pi}$ in agreement with Erdogan and Gupta's previous work [8].

The use of Fig. 15 can be elucidated by considering the example of $E_f/E_s = 28$ again. Substrate is under uniform tensile stress, σ^0, so that Eqs. (8), (9) and (12) yield $f = \sigma^0\pi/2$. Thin film has a profile given by Eq. (14) with the shape parameter $\nu = 0.9$. If the aspect ratio, a/b_0, is taken as 16 (the stress distribution for this case was already given in Fig. 10), χ is calculated to be 0.286 from Eq. (16). The corresponding $K_{II}/f\sqrt{a}$ is found to be 0.47 from Fig. 15 (point A), and hence $K_{II} = 0.74\,\sigma^0\sqrt{a}$. If the aspect ratio is increased to 160 (point B), K_{II} is found to be $K_{II} = 0.31\,\sigma^0\sqrt{\sqrt{a}}$.

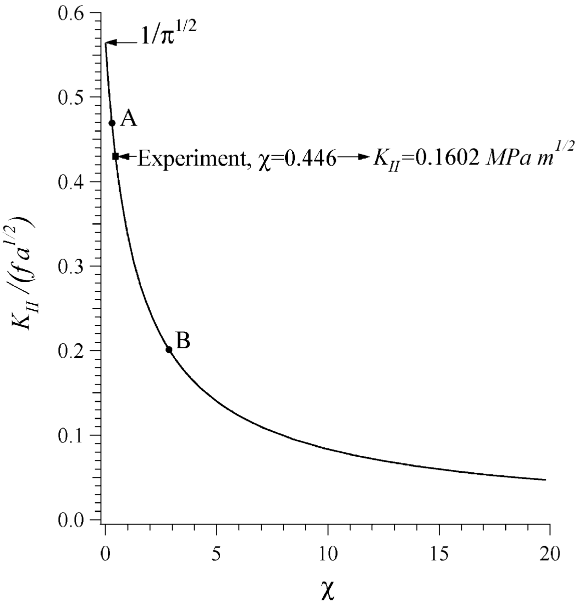

Fig. 15. Plot of K_{II} normalized by $f\sqrt{a}$ vs the dimensionless parameter χ incorporating material mismatch and film dimensions according to Eq. (16). f represents a variety of loading conditions according to Eqs. (8), (9), (10) and (12). When $\chi = 0$, $K_{II}/(f\sqrt{a})$ has its maximum value of $1/\sqrt{\pi}$. Point A corresponds to $E_f/E_s = 28$ where the aspect ratio, a/b_0, of the thin film is 16. When this is increased to 160, one obtains a decrease in the stress intensity factor as shown by Point B. Based on the experimental measurements of Fig. 4, K_{II} is determined to be 0.1602 MPa$\sqrt{\text{m}}$ at the onset of delamination for that particular Al–polyimide interface.

Furthermore, theory and experimental measurements can be incorporated for the determination of critical stress intensity factors for delamination. To demonstrate this, let us go back to the uniaxial experiment with the Al-coated polyimide specimen, where, as mentioned in the section devoted to experimental results, delamination of the Al film can be observed via in-situ microscopy. In this particular experiment, delamination takes place at the edge of 20 μm-wide Al strips, i.e. $a = 10$ μm and $b_0 = 0.4$ μm, when the far-field stress reaches 75 MPa. With this geometry and material mismatch, χ is found to be 0.446. Using this value in Fig. 15, one finds $K_{II} = 0.1602$ MPa$\sqrt{\text{m}}$ at the onset of delamination.

Finally, the same procedure can be applied to a case where thermal residual stress is the driving force for edge debond. This time, the forcing function F of Eq. (12) is given by Eq. (10). Due to the linearity of the problem, K_{II} for thermal and mechanical loading can be added to obtain the resultant K_{II}.

6. Conclusion

This work reports interfacial shear stress calculations between a rectangular strip of thin film and its substrate in closed form. The solution exhibits square root singularity near the free edges, and this can be utilized to explain the initiation of edge debond. Singular behavior is characterized using the notion of the stress intensity factor, K_{II}, which is solved in closed form. For a given loading, K_{II} decreases with increasing ratio of film length to film thickness, i.e. for a fixed film length, a thinner film will be more unlikely to fail by edge debonding compared to a thicker one. K_{II} also decreases with decreasing film-to-substrate stiffness ratio. These trends are governed by a single, dimensionless parameter that incorporates material mismatch and film dimensions. It is also shown that as long as the film stiffness is at least ten times bigger than that of the substrate, bending effects are negligible and hence, model predictions become accurate. Finally, measurements from tensile experiments conducted on Al-coated polyimide samples are used to calculate the critical stress intensity factor for that particular interface.

Acknowledgements

Authors gratefully acknowledge the support of DARPA under contract DABT63-97-C-0069. Microscopy was carried out in the Center for Microanalysis of Materials, University of Illinois, which is supported by the U.S. Department of Energy under grant: DEFG02-96ER-45439. Professor Shannon is thanked for supplying tension specimens.

Appendix A

Solution of the compatibility equation

The compatibility equation is converted to the following Fredholm equation of the second kind:

$$\Gamma(x)-\int_{-a}^{a} K(x,\sigma)\Gamma(\sigma)\mathrm{d}\sigma = g(x) \tag{A1}$$

The right-hand side of this equation, $g(x)$, is given by the following expression:

$$g(x) = g_0(x)-\frac{\cos\theta(x)}{\cos\theta(a)}g_0(a) \tag{A2}$$

with $g_0(x)$ defined as

$$g_0(x) = -\frac{f}{\pi}\int_0^x\left(\sin[\theta(t)-\theta(x)] + \frac{t\cos[(\theta(t)-\theta(x)]}{\sqrt{a^2-t^2}}\right)\mathrm{d}t \tag{A3}$$

where

$$\theta(x) = \frac{1}{\pi A}\int_0^x\frac{1}{b(t)}\mathrm{d}t \tag{A4}$$

The rectangular film profile is approximated by the following formula:

$$b(x) = b_0\sqrt{1-\frac{x^2}{a^2}}\left(1 + \nu\frac{x^2}{a^2}\right) \tag{A5}$$

where the shape parameter $\nu = 0.9$.

With this particular thickness profile, $K(x,t)$ and the function $\theta(x)$ are given by

$$K(x,t) = \frac{(\chi/\pi)\nu t}{a^2 + \nu t^2}\varphi_1(x) + \frac{(\chi/\pi)\nu}{a^2 + \nu t^2}\varphi_2(x) \tag{A6}$$

where

$$\varphi_k(x) = \int_0^x\frac{\cos[\theta(\sigma)-\theta(x)]}{\sqrt{a^2-\sigma^2}}\,\frac{\sigma^{k-1}}{1 + \nu\frac{\sigma^2}{a^2}}\mathrm{d}\sigma \tag{A7}$$

$$-\frac{\cos\theta(x)}{\cos\theta(a)}\int_0^a\frac{\cos[\theta(\sigma)-\theta(a)]}{\sqrt{a^2-\sigma^2}}\,\frac{\sigma^{k-1}}{1 + \nu\frac{\sigma^2}{a^2}}\mathrm{d}\sigma$$

and

$$\theta(x) = \frac{\chi}{\sqrt{1 + \nu}}\arctan\frac{x\sqrt{1 + \nu}}{\sqrt{a^2-x^2}} \tag{A8}$$

with

$$\chi = \frac{1}{2m}\frac{a}{b_0},\ m = \frac{E_\mathrm{f}}{E_\mathrm{s}}\frac{1-\nu_\mathrm{s}^2}{1-\nu_\mathrm{f}^2} \tag{A9}$$

Using these functions, the Fredholm equation can be solved algebraically for $\Gamma(x)$ and $\Gamma(x)$ is given by the following expression:

$$\Gamma(x) = g(x) + \frac{\frac{\chi}{\pi}\nu\int_{-a}^{a}\frac{g(\sigma)}{a^2 + \nu\sigma^2}\mathrm{d}\sigma}{1-\frac{\chi}{\pi}\nu\int_{-a}^{a}\frac{\varphi_2(\sigma)}{a^2 + \nu\sigma^2}\mathrm{d}\sigma}\varphi_2(x) \tag{A10}$$

Appendix B

List of I_i and C_i

$$\xi = x/a$$

$$\theta(\xi) = \frac{\chi}{\sqrt{1 + \nu}}\arctan\frac{\xi\sqrt{1 + \nu}}{\sqrt{1-\xi^2}}$$

$$I_1(\xi) = \int_0^\xi\left(-\cos[\theta(\varrho)-\theta(\xi)] + \frac{\varrho\sin[\theta(\varrho)-\theta(\xi)]}{\sqrt{1-\varrho^2}}\right)\mathrm{d}\varrho$$

$$I_2 = \int_0^1\left(\sin\left[\theta(\varrho)-\frac{\chi}{\sqrt{1 + \nu}}\frac{\pi}{2}\right]\right.$$

$$+\frac{\varrho\cos\left[\theta(\varrho)-\frac{\chi}{\sqrt{1+\nu}}\frac{\pi}{2}\right]}{\sqrt{1-\varrho^2}}\Bigg)\mathrm{d}\varrho$$

$$I_3(\xi)=\int_0^{\xi}\frac{\varrho\sin[\theta(\varrho)-\theta(\xi)]}{\sqrt{1-\varrho^2}(1+\nu\varrho^2)}\mathrm{d}\varrho$$

$$I_4=\int_0^1\frac{\varrho\cos\left[\theta(\varrho)-\frac{\chi}{\sqrt{1+\nu}}\frac{\pi}{2}\right]}{\sqrt{1-\varrho^2}(1+\nu\varrho^2)}\mathrm{d}\varrho$$

$$C_1=\frac{\chi\nu}{\pi}\left[\int_{-1}^{1}\frac{1}{1+\nu\varrho^2}I_5(\varrho)\mathrm{d}\varrho-\frac{I_2I_6}{\cos\left[\frac{\chi}{\sqrt{1+\nu}}\frac{\pi}{2}\right]}\right]$$

$$I_5(\varrho)=\int_0^{\varrho}\left(\sin[\theta(\iota)-\theta(\varrho)]+\frac{\iota\cos[\theta(\iota)-\theta(\varrho)]}{\sqrt{1-\iota^2}}\right)\mathrm{d}\iota$$

$$I_6=\int_{-1}^{1}\frac{\cos[\theta(\iota)]}{1+\nu\iota^2}\mathrm{d}\iota$$

$$C_2=1-\frac{\chi\nu}{\pi}\left[\int_{-1}^{1}\frac{I_7(\varrho)}{1+\nu\varrho^2}\mathrm{d}\varrho-\frac{I_4I_6}{\cos\left[\frac{\chi}{\sqrt{1+\nu}}\frac{\pi}{2}\right]}\right]$$

$$I_7(\varrho)=\int_0^{\varrho}\frac{\iota\cos[\theta(\iota)-\theta(\varrho)]}{\sqrt{1-\iota^2}(1+\nu\iota^2)}\mathrm{d}\iota \qquad \text{(B1)}$$

References

[1] Bagchi A, Lucas GE, Suo Z, Evans AG. J Mater Res 1994;9(7):1734.
[2] Chiu SL, Leu J, Ho PS. J Appl Phys 1994;76(9):5136.
[3] Ogawa S, Cho H, Yamanaka K, Takemoto M. JSME Int J, Series A 1998;41(3):446.
[4] Akisanya AR, Fleck NA. Int J Solids Structures 1994;31(23):3175.
[5] Yu HH, He MY, Hutchinson JW. Acta Mater 2001;49(1):93.
[6] Liu XH, Suo Z, Ma Q. Acta Mater 1999;47(1):67.
[7] Klingbeil NW, Beuth JL. Eng Fracture Mech 2000;66(2):111.
[8] Erdogan F, Gupta GD. J Appl Mech 1971;38(4):937.
[9] Hein VL, Erdogan F. Int J Fracture Mech 1971;7(3):317.
[10] Bogy DB. Int J Solids Structures 1970;6:1287.
[11] Tilscher M, Munz D, Yang YY. J Adhesion 1995;49:1.
[12] Akisanya AR, Fleck NA. Int J Solids Structures 1997;34(13):1645.
[13] Jiang ZQ, Huang Y, Chandra A. J Electron Pkg'g 1997;119:127.
[14] Shield TW, Kim KS. Int J Solids Structures 1992;29(9):1085.
[15] Muskhelishvili NI. Singular integral equations, 2nd ed. Groningen: P. Noordhoff NV, 1953.
[16] Vekua IN. Prikladnaia Matematika i Mekhanika 1945;9(2):143.
[17] Saif MTA, Alaca BE, Sehitoglu H. IEEE J Microelectromech Syst 1999;8(3):335.
[18] Agrawal DC, Raj R. Acta Metall 1989;37(4):1265.
[19] Saif MTA, Hui CY, Zehnder AT. Thin Solid Films 1993;224:159.
[20] Getting Started with ABAQUS/Standard. USA: Hibbitt, Karlsson & Sorensen, Inc, 1996.